Broadband imaging via direct inversion of blended dispersed source array data

Caporal, Matteo; Blacquière, Gerrit; Davydenko, Mikhail

DOI
10.1111/1365-2478.12584

Publication date
2018

Document Version
Final published version

Published in
Geophysical Prospecting

Geophysical Prospecting

EAGE EUROPEAN ASSOCIATION OF GEOSCIENTISTS & ENGINEERS

Geophysical Prospecting, 2018, **66**, 942–953 doi: 10.1111/1365-2478.12584

Broadband imaging via direct inversion of blended dispersed source array data

Matteo Caporal[1]*, Gerrit Blacquière[1] and Mikhail Davydenko[2]

[1]*Faculty of Civil Engineering and Geosciences, Delft University of Technology, 2628 CN Delft, The Netherlands, and* [2]*Faculty of Applied Physics, Delft University of Technology, 2628 CJ Delft, The Netherlands*

Received December 2016, revision accepted September 2017

ABSTRACT

Although seismic sources typically consist of identical broadband units alone, no physical constraint dictates the use of only one kind of device. We propose an acquisition method that involves the simultaneous exploitation of multiple types of sources during seismic surveys. It is suggested to replace (or support) traditional broadband sources with several devices individually transmitting diverse and reduced frequency bands and covering together the entire temporal and spatial bandwidth of interest. Together, these devices represent a so-called dispersed source array.

As a consequence, the use of simpler sources becomes a practical proposition for seismic acquisition. In fact, the devices dedicated to the generation of the higher frequencies may be smaller and less powerful than the conventional sources, providing the acquisition system with increased operational flexibility and decreasing its environmental impact. Offshore, we can think of more manageable boats carrying air guns of different volumes or marine vibrators generating sweeps with different frequency ranges. On land, vibrator trucks of different sizes, specifically designed for the emission of particular frequency bands, are preferred. From a manufacturing point of view, such source units guarantee a more efficient acoustic energy transmission than today's complex broadband alternatives, relaxing the low- versus high-frequency compromise. Furthermore, specific attention can be addressed to choose shot densities that are optimum for different devices according to their emitted bandwidth. In fact, since the sampling requirements depend on the maximum transmitted frequencies, the appropriate number of sources dedicated to the lower frequencies is relatively small, provided the signal-to-noise ratio requirements are met. Additionally, the method allows to rethink the way to address the ghost problem in marine seismic acquisition, permitting to tow different sources at different depths based on the devices' individual central frequencies. As a consequence, the destructive interference of the ghost notches, including the one at 0 Hz, is largely mitigated. Furthermore, blended acquisition (also known as simultaneous source acquisition) is part of the dispersed source array concept, improving the operational flexibility, cost efficiency, and signal-to-noise ratio.

Based on theoretical considerations and numerical data examples, the advantages of this approach and its feasibility are demonstrated.

Key words: Acquisition, Seismic, Inversion.

*E-mail: m.caporal@tudelft.nl

INTRODUCTION

In exploration seismology, it is widely accepted that the contribution of both high and low frequencies is of fundamental importance for high-quality seismic imaging. High frequencies provide sharper wavelets resulting in an improved vertical resolution. Low frequencies can drastically reduce the amplitude of wavelet side lobes and therefore the potential interference among neighboring seismic events. They also translate in better signal penetration, suffering less from scattering and attenuation. Furthermore, they play a crucial role in seismic inversion for velocity and impedance models. An interesting and detailed overview on the importance of broadband data acquisition and processing, with specific focus on low frequencies, is presented by ten Kroode *et al.* (2013).

In particular, the most commonly used seismic sources, both on land (vibroseis, dynamite) and offshore (air guns), produce relatively little low-frequency energy. The conventional methodology to acquire satisfactory data in the whole bandwidth of interest consists of producing more energy at all frequencies utilising broadband sources. From a practical point of view, a significant effort is required to profitably manufacture and operate such sources, and it is often unavoidable to accept a trade-off between desired bandwidth and system engineering efficiency.

Following the guidelines drawn by Berkhout (2012), we propose to employ more than one type of source during the same seismic survey, together representing a dispersed source array (DSA). Each source unit involved in the acquisition might be dedicated to a particular frequency bandwidth without the need to satisfy the seismic wideband requirement, thus avoiding the abovementioned trade-off. As a whole, the ensemble of sources incorporated in the array is designed to cover the entire temporal and spatial bandwidth of interest.

The employment of low-frequency sources in seismic acquisition has also been proposed by Reust *et al.* (2015) and Dellinger *et al.* (2016), mainly as a supplement to conventional broadband acquisition. On the other hand, an interesting first experiment of DSA land data acquisition and inversion (designed for Full Waveform Inversion application) has been carried out and presented by Tsingas, Kim and Yoo (2016), utilising standard vibrators.

The DSA concept could enhance the operational flexibility of the system, since for the higher frequencies, we could think of utilising much smaller devices. Such devices are allowed to be less powerful, emitting only the required amount of energy, provided the signal-to-noise requirements are met. This characteristic would also make them more suitable to comply with strict regulations that apply in marine environment. Additionally, dedicated source intervals and source depths can be adopted for each type of device with beneficial implications. In the following sections, these benefits are studied in detail. A brief theoretical illustration of the DSA concept and a numerical example of 3D blended DSA data migration are also provided.

BENEFITS OF DISPERSED SOURCE ARRAY ACQUISITIONS

To illustrate the concept, we utilised four different source unit types: *ultralow-* (from 2 to 6 Hz), *low-* (from 5 to 15 Hz), *mid-* (from 10 to 30 Hz), and *high*-frequency sources (from 20 to 60 Hz). Note that each source type spans a frequency bandwidth corresponding to the same number of octaves. In such situation, given bandwidths are partially overlapping for a relatively small range of frequencies. This characteristic will simplify the treatment of the data for both deblending (i.e., source separation) and direct processing. In Fig. 1, the amplitude spectra of aforementioned sources are shown (top). Corresponding examples of acoustic energy propagation in a homogeneous medium, together with the relative source wavelets, are presented (bottom). It is worth observing that the spectral characteristics of the proposed sources are designed to guarantee flat amplitude conditions in the whole frequency band of interest. Nevertheless, as long as the signal-to-noise ratio is acceptable, this is not essential.

In the following paragraphs, a description of the main benefits of DSA acquisition systems is provided. For simplicity, they have been divided in four different categories and discussed separately.

Sampling issues

It is well known that alias-free spatial sampling (both on the source and on the receiver side) is achieved when the maximum wave numbers of interest are properly sampled (Niland 1989). This means that the spatial sampling Δx is required to satisfy the following inequality:

$$\Delta x < \frac{c_{\min}}{2 f_{\max} \sin \theta_{\max}}, \tag{1}$$

where $c_{\min}$ is the minimum propagation velocity, whereas $f_{\max}$ and $\theta_{\max}$ are the maximum frequency and the maximum angle of the signal we aim to record, respectively. In other words, the sampling interval should be smaller than a half-period of the minimum horizontal wave length, in order to allow an accurate reconstruction of the wavefields.

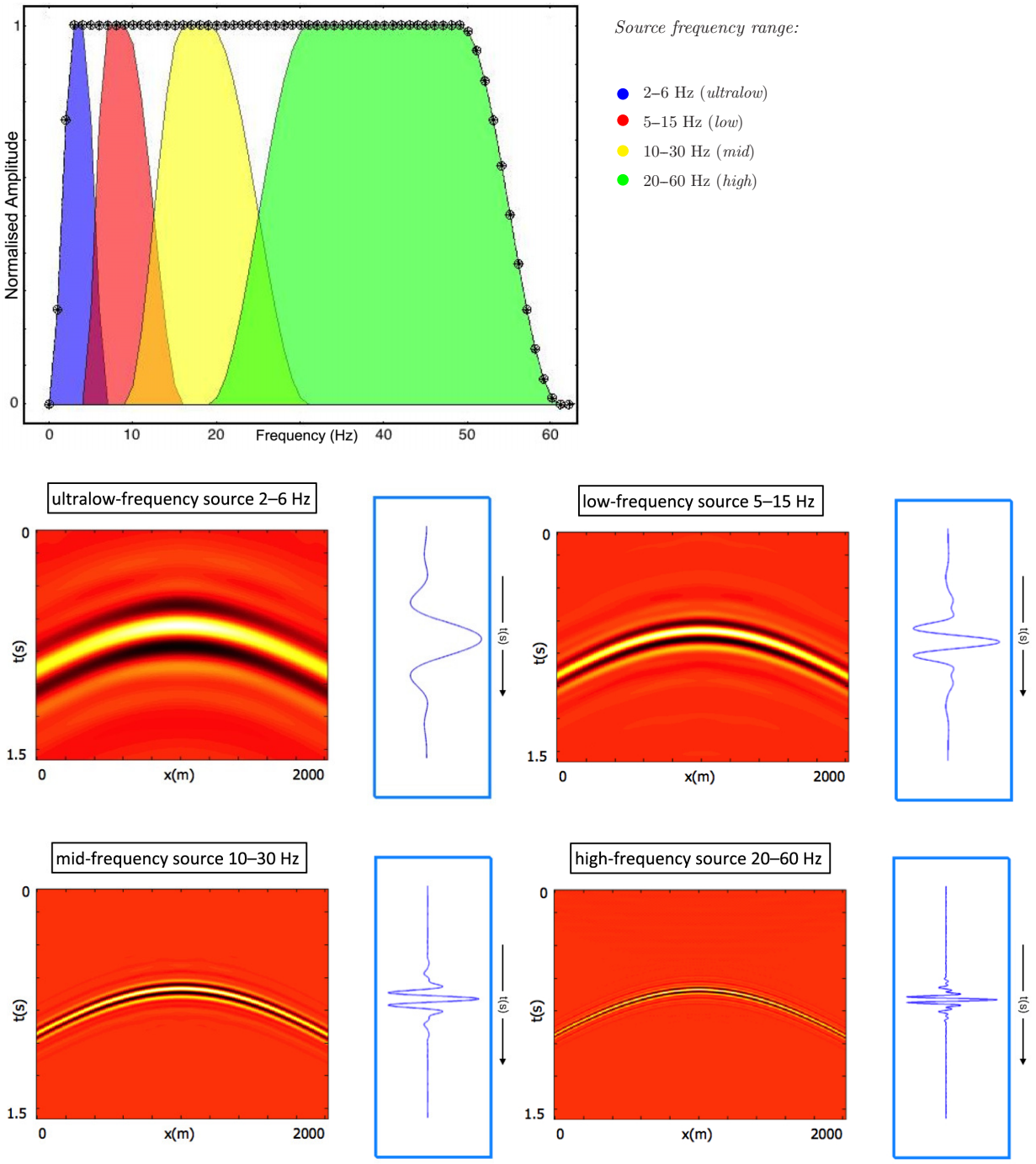

Figure 1 Amplitude spectra corresponding to chosen source units (top). Examples of DSA acoustic energy propagation in a homogeneous medium and corresponding source wavelets (bottom).

Within DSA acquisition systems, each different source type has therefore specific sampling requirements. In particular, DSA acquisition systems could give us the chance to avoid oversampling on the lower frequency side and undersampling on the higher frequency side. In fact, the required number of source units (and shots) producing the lower significant frequencies is relatively small, provided that the signal-to-noise ratio is acceptable. Note that, regarding the

low and ultralow frequencies, current acquisition geometries are excellent or even too dense, as far as spatial sampling is concerned.

Technical advantages

From a technical point of view, we believe that DSA acquisition has the potential to relax the low- versus high-frequency compromise. Addressing specific attention to the manufacture of different source units might in fact drastically improve their signal emission properties and simplify their design and production. Modern multiple-driver loudspeaker systems are based on the same key concept, and their improved performances are demonstrated and widely accepted (see, e.g., Davis and Patronis 2006). Furthermore, except for the very low frequencies of seismic interest, the conventional sources are significantly bigger and louder than required (Laws, Kragh and Morgan 2008; Kragh *et al.* 2012). The same applies to modern loudspeaker systems: the drivers dedicated to the reproduction of the high audible frequencies (tweeters) are considerably smaller than the drivers dedicated to the reproduction of the low frequencies (woofers).

Besides, the recent advances in unmanned systems technology and the improved operational flexibility enabled by the smaller dimensions of most DSA devices may be beneficial to data acquisition efficiency. With DSAs, the use of relatively simple autonomous devices becomes a practical proposition for seismic surveys. In a marine environment, we might consider utilising several autonomous source boats at the same time. On land, a combination of autonomous vibroseis trucks of varied dimensions and designs is suggested. An introductory overview on this proposition is presented by Caporal, Blacquière and Davydenko (2016).

Ghost matching

In the marine environment, seismic sources such as air gun arrays are towed at some depth z_s below the water surface. Consequently, the source wavefield travels not only downwards but also upwards towards the air–water interface. Such interface can be considered a virtually perfect reflector with a reflection coefficient very close to -1. Thus, a secondary source is scattered back and travels downwards, delayed in time, and reversed in polarity with respect to the primary. By optical analogy, aforementioned secondary source is referred to as *source ghost* and can be considered as a particular form of natural blending. For a more exhaustive explanation of the ghost problem, the reader is referred to Parkes and Hatton (1986). Hereafter, we will refer to the total transmitted signal as a *composite wavefield* (sum of the primary and the source ghost). The time delay between the two different acoustic wavefields is equal to $\frac{2z_s cos\Phi}{c_w}$, where Φ is the angle of incidence at the water surface and c_w is the velocity of sound in the water layer. Clearly, if $2nz_s cos\Phi$ is equal to half a wavelength (with $n \in \mathbf{Z}$), the primary and source ghost wavefields will add constructively. On the other hand, if $2nz_s cos\Phi$ is equal to a full wavelength, the primary and source ghost wavefields will add destructively, requiring the use of dedicated techniques to recover lost information. Note that, in case of rough weather conditions, additional precautions need to be taken during the processing or inversion steps in order to properly address the ghost problem. In fact, the assumption of a virtually perfect reflection from the sea surface would not hold anymore. Considerable research has been and is currently conducted on this topic (e.g., Laws and Kragh 2002; Amundsen *et al.* 2005; Orji, Söllner and Gelius 2012).

For what concerns DSAs, extra benefits arise if we look at the ghost issue. To reduce the effect of the source ghost, we can place each source type at the optimum depth below the water surface, i.e., at $z_s = \frac{(2n+1)\lambda_c}{4}$, one quarter of its central frequency wavelength λ_c (or at any half wavelength starting from that value). We will call this procedure *ghost matching*. This effect is illustrated in Figs. 2 and 3. A 2D comparison between the composite wavefields generated by devices towed at shallow, optimum, and deep levels below the water surface is shown (in the $f - k_x$ domain) for each source type including an ideal full-band unit (Fig. 2). Here, with full band, we refer to the entire bandwidth under consideration. The wavefield given by the sum of contributions of all DSA sources is also presented (Fig. 3). Clearly, in the case of shallow tow depths, the signal is greatly attenuated. When sources are towed too deep, undesired ghost notches appear in the spectrum. The DSA concept allows us to reduce both complications: ghost destructive interference and notches are largely avoided, and low frequency attenuation due to a too shallow tow depth can be prevented. As a result, the ghost wavefield will enhance the signal instead of compromising it, requiring simpler or no deghosting algorithms to be deployed. The overall result is definitely improved also with respect to the composite wavefield generated by the full-band device towed at its optimum depth. We could see this proposal as an optimised extension of the multilevel source arrays concept already widely developed and tested in the oil industry (see, for an overview, Shen *et al.* 2014).

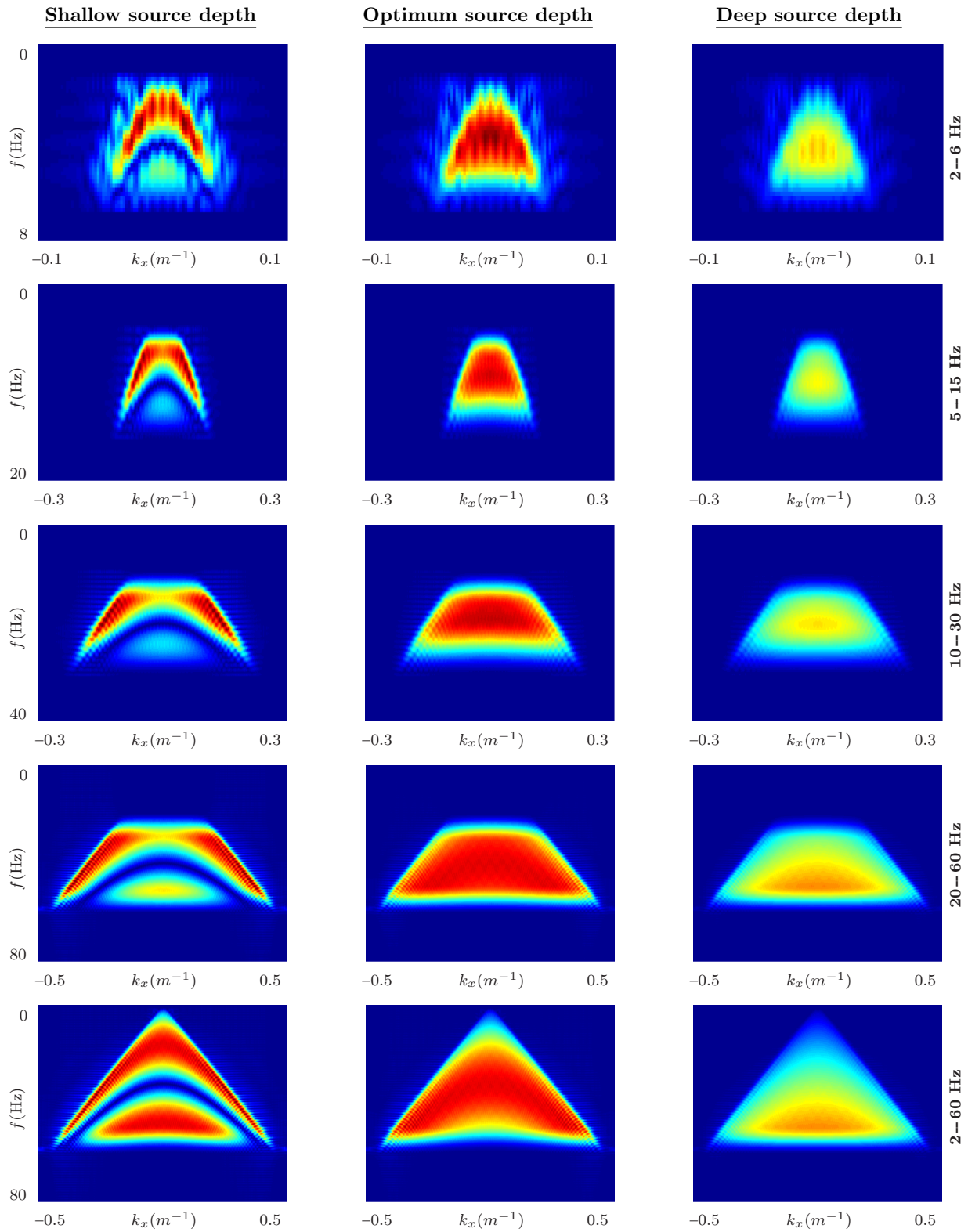

Figure 2 Comparison, in the $f - k_x$ domain, between the composite wavefields generated by devices towed at shallow, optimum, and deep levels below the water surface for each source type including an ideal full-band unit.

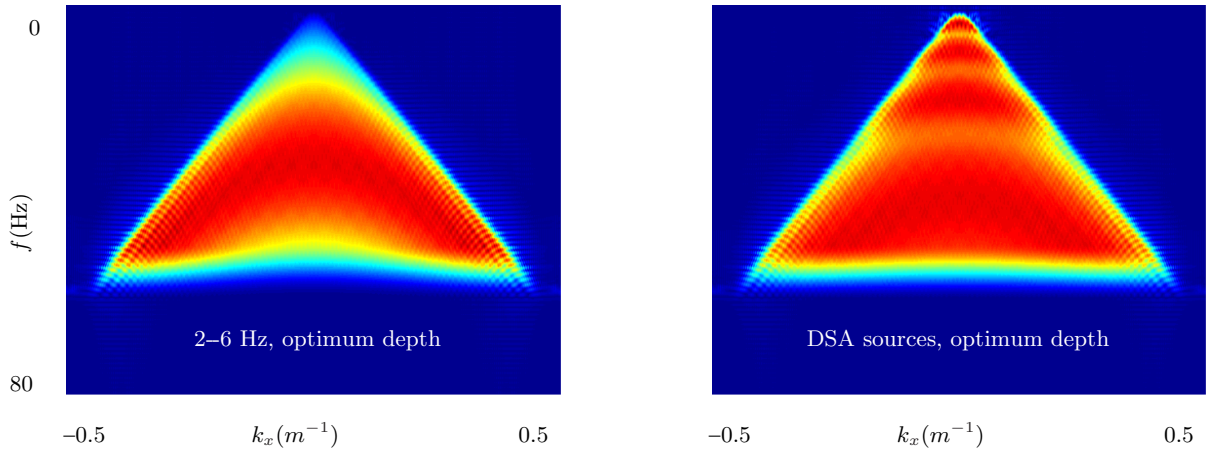

Figure 3 Comparison, in the $f - k_x$ domain, between the composite wavefields generated by an ideal full-band unit towed at optimum depth and the the wavefield given by the sum of the contributions of all DSA sources at optimum depths.

Marine environmental issues

In the last few decades, the increasing awareness and concern towards anthropologically driven environmental changes have significantly affected the way marine seismic surveys are designed. Despite that important aspects of underwater bioacoustics remain unresolved, a growing number of studies have been conducted on the impact of anthropogenic noise on marine fauna (see, for an overview, Nowacek *et al.* 2007; Laiolo 2010; Erbe *et al.* 2016; Kunc, McLaughlin and Schmidt 2016; Shannon *et al.* 2016). Here, with anthropogenic noise, we refer to all sound produced by human activities, including seismic surveys. In particular, most common undesired and potentially negative responses to acoustic emissions due to seismic sources include acoustic masking (Tanner 1958) and seemingly temporary changes in behaviour of marine species. Considering the complexity of ecosystem processes, the understanding of how immediate individual responses translate in large-scale and long-term ecological effects is currently limited. Nevertheless, the research carried on thus far has led to a considerable tightening of the regulations on aquatic life protection (European Union 2008; MSFD 2014; NOAA 2016).

De facto, the critical parameter to take into consideration while planning a seismic survey is the signal-to-noise ratio. Here, with noise, we refer to the recorded signal, which is unrelated to the reflection response of the controlled emitted sound. It is therefore crucial to acknowledge that there is no generally suitable set of rules to improve the final result or to decrease the environmental impact. For instance, it is recommended to perform seismic source testing during the preliminary phases of the survey in order to assess the minimal signal strength for the area under consideration. Geological and ecological prior information may also be beneficial in this regard. It has indeed been demonstrated that in several cases, within the bandwidth of interest, the seismic source is unnecessarily too loud (Laws *et al.* 2008; Fontana and Zickerman 2010). Additionally, conventional impulsive sources, such as air guns, produce a significant amount of energy at frequency ranges that are of no benefit to seismic imaging but could potentially be harmful to aquatic life (Madsen *et al.* 2006; Nowacek *et al.* 2007). Specifically, the frequency band of seismic interest (<150 Hz) constitutes a threat to a relatively small subset of marine fauna (Southall *et al.* 2007). Note that higher frequencies considerably contribute to the total emitted energy, which is often the main parameter taken into consideration by regulators. New types of air guns have been recently designed in order to decrease the acoustic output at non-relevant frequencies without compromising the pulse shape within the seismic frequency range (Coste *et al.* 2014). A greater benefit would result from the deployment of marine seismic vibrators in place of impulsive sources. See Duncan *et al.* (2017) for a realistic modeling comparison between received sound levels produced by a marine vibrator array and those from an air gun array under some typical survey scenarios. In light of these considerations, we are further motivated to carry our research on DSA forward given their flexibility in terms of signal frequency emission.

THEORETICAL FRAMEWORK

In the following, wavefield extrapolation-based modelling and inversion will be briefly discussed by means of the so-called

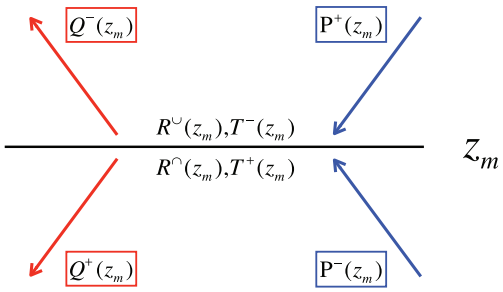

Figure 4 Incoming (P) and outgoing (Q) fields at depth level z_m.

WRW model, introduced by Berkhout (1982). Instructions on how to extend this scheme to the description of blended and dispersed source array (DSA) acquisition systems are given. Note that a dataset is considered to be blended when individual responses from different sources are overlapping in space, time, and both spatial and temporal frequencies (Berkhout 2008). The domain of reference for the following theoretical consideration is the space–frequency domain. Expressions are valid for stationary receiver geometries. In Table 1, a description of the notation is provided. Each matrix and operator introduced below refer to a single monochromatic component of the fields.

Theoretical framework: modelling

At each depth level, the total outgoing wavefield can be represented as the sum of the transmitted incoming wavefield in the same propagation direction and the wavefield reflected from the opposite direction (see Fig. 4), as follows:

$$\mathbf{Q}^+(z_m) = \mathbf{T}^+(z_m)\mathbf{P}^+(z_m) + \mathbf{R}^\cap(z_m)\mathbf{P}^-(z_m), \tag{2}$$

$$\mathbf{Q}^-(z_m) = \mathbf{T}^-(z_m)\mathbf{P}^-(z_m) + \mathbf{R}^\cup(z_m)\mathbf{P}^+(z_m), \tag{3}$$

where

$$\mathbf{T}^\pm(z_m) = \mathbf{I} + \delta\mathbf{T}^\pm(z_m). \tag{4}$$

From the above, it follows that

$$\mathbf{Q}^+(z_m) = \mathbf{P}^+(z_m) + \delta\mathbf{T}^+(z_m)\mathbf{P}^+(z_m) + \mathbf{R}^\cap(z_m)\mathbf{P}^-(z_m), \tag{5}$$

$$\mathbf{Q}^-(z_m) = \mathbf{P}^-(z_m) + \delta\mathbf{T}^-(z_m)\mathbf{P}^-(z_m) + \mathbf{R}^\cup(z_m)\mathbf{P}^+(z_m). \tag{6}$$

Note that the last two additional terms on the right of both equations account for the scattering effects and can be considered as secondary sources $\delta\mathbf{S}^\pm(z_m$; Berkhout 2014a), as follows:

$$\delta\mathbf{S}^+(z_m) = \delta\mathbf{T}^+(z_m)\mathbf{P}^+(z_m) + \mathbf{R}^\cap(z_m)\mathbf{P}^-(z_m), \tag{7}$$

$$\delta\mathbf{S}^-(z_m) = \delta\mathbf{T}^-(z_m)\mathbf{P}^-(z_m) + \mathbf{R}^\cup(z_m)\mathbf{P}^+(z_m). \tag{8}$$

If we now assume small shear contrast at the interface (i.e., we neglect wave conversion), we have the following:

$$\mathbf{R}^\cup(z_m) = -\mathbf{R}^\cap(z_m); \quad \mathbf{R}^\cup(z_m) = \delta\mathbf{T}^+(z_m); \quad \mathbf{R}^\cap(z_m) = \delta\mathbf{T}^-(z_m). \tag{9}$$

Thus,

$$\delta\mathbf{S}^-(z_m) = \delta\mathbf{S}^+(z_m) = \delta\mathbf{S}(z_m). \tag{10}$$

We can, therefore, rewrite equations 5 and 6 as follows:

$$\mathbf{Q}^+(z_m) = \mathbf{P}^+(z_m) + \delta\mathbf{S}(z_m), \tag{11}$$

Table 1 Overview of used notations

Notation	Description
z_m	denotes the mth depth level. Index increases with depth.
$\mathbf{S}(z_m)$	is the source wavefield at depth level z_m. Key amplitude and phase information about the spectral properties of the different DSA sources is therefore enclosed here. Each column represents one source (or source array). Each row corresponds to a different spatial coordinate.
$\mathbf{P}(z_m)$	is the incoming wavefield at depth z_m. In other words, it is the pressure wavefield registered at the given depth level.
$\mathbf{Q}(z_m)$	is the outgoing wavefield at depth z_m. In other words, it is the pressure wavefield leaving the given depth level.
$\mathbf{R}(z_m)$	is the reflectivity operator describing the scattering occurring at depth z_m. Namely, it specifies how the incident wavefield is converted into the reflected wavefield.
$\mathbf{T}(z_m)$	is the full transmission operator at depth z_m. It can be represented as the sum of a unity matrix $\mathbf{I}$ and an additional term $\delta\mathbf{T}$.
$\delta\mathbf{T}(z_m)$	is the differential transmission operator at depth z_m.
$\mathbf{W}(z_l, z_r)$	is the one-way propagation operator. Each column contains a discretised Rayleigh II operator (Berkhout 1982), being the vertical derivative of a Green's function and describing the wave propagation between depth levels z_r and z_l.
$*^{+,-}$	denote the wavefield direction (downgoing +, upgoing -).
$*^{\cup,\cap}$	denote the direction towards which the wavefield is reflected (down ∩, up ∪).
$*^H$	denotes the conjugate transpose of a matrix.

$$\mathbf{Q}^{-}(z_m) = \mathbf{P}^{-}(z_m) + \delta\mathbf{S}(z_m). \tag{12}$$

After propagation, the total outgoing wavefields become incoming wavefields at the neighboring depth levels, as follows:

$$\mathbf{P}^{+}(z_m) = \mathbf{W}^{+}(z_m, z_{m-1})\mathbf{Q}^{+}(z_{m-1}), \tag{13}$$

$$\mathbf{P}^{-}(z_m) = \mathbf{W}^{-}(z_m, z_{m+1})\mathbf{Q}^{-}(z_{m+1}). \tag{14}$$

This leads us to the following:

$$\mathbf{P}^{+}(z_m) = \mathbf{W}^{+}(z_m, z_0)\mathbf{S}^{+}(z_0) + \sum_{n>0}\mathbf{W}^{+}(z_m, z_n)\delta\mathbf{S}(z_n), \tag{15}$$

$$\mathbf{P}^{-}(z_0) = \sum_{n>0}\mathbf{W}^{-}(z_0, z_n)\delta\mathbf{S}(z_n). \tag{16}$$

Note that all sources and receivers are assumed to be at depth level z_0.

By utilising this scheme, the wavefield resulting from several round trips (from the surface to an arbitrary depth level z_M and back) includes primary reflections, internal multiples, and also transmission effects. Physically, the surface multiples can also be included, if the total upgoing wavefield at the surface is reinjected, after multiplication with the free surface reflectivity as an additional downgoing wavefield. Thus, each further round trip can be described as an increment of the scattering order of the wavefield. Using this modelling approach, the so-called full wavefield modelling (FWMod, see Berkhout 2014a), we can therefore effectively add to the modelled data as many orders of multiples as necessary.

Theoretical framework: inversion

The so-called full wave migration algorithm (see Berkhout 2014b; Davydenko and Verschuur 2017) aims at minimising, by iteratively updating the reflectivities, the difference between the observed data and the data modelled with the aforementioned FWMod method. A schematic representation of the inversion loop is presented in Fig. 5. The objective function can be described as follows:

$$J = J_{\Delta} + f(\mathbf{R}), \tag{17}$$

where the term $f(\mathbf{R})$ is a penalty function chosen based on an arbitrary constraining function. The term J_{Δ} is a misfit norm function of the following form:

$$J_{\Delta} \quad = \quad \sum_{\omega}\left\|\Delta\mathbf{P}(z_0)\right\|_2^2 \quad = \quad \sum_{\omega} Tr\left(\Delta\mathbf{P}(z_0)\Delta\mathbf{P}^{H}(z_0)\right), \tag{18}$$

where $\Delta\mathbf{P}(z_0)$ is the residual, i.e., the difference between the observed data $\mathbf{P}_{obs}(z_0)$ and the modelled data $\mathbf{P}^{-}_{mod}(z_0)$, as follows:

$$\Delta\mathbf{P}(z_0) \quad = \quad \mathbf{P}_{obs}(z_0) - \mathbf{P}^{-}_{mod}(z_0). \tag{19}$$

According to Petersen and Pedersen (2012), the following derivative property holds while dealing with the derivative of matrix traces:

$$\frac{\partial}{\partial\mathbf{X}} Tr[(\mathbf{AXB}+\mathbf{C})(\mathbf{AXB}+\mathbf{C})^{H}] = 2\mathbf{A}^{H}(\mathbf{AXB}+\mathbf{C})\mathbf{B}^{H}. \tag{20}$$

In our case,

$$\mathbf{AXB} + \mathbf{C} = \Delta\mathbf{P}(z_0); \tag{21}$$

$$\mathbf{A} = -\sum_{n>0}\mathbf{W}^{-}(z_0, z_n); \tag{22}$$

$$\mathbf{X} = \mathbf{R}^{\cup}(z_n); \tag{23}$$

$$\mathbf{B} = \mathbf{P}^{+}_{mod}(z_n); \tag{24}$$

$$\mathbf{C} = \mathbf{P}_{obs}(z_0) - \sum_{n>0}\mathbf{W}^{-}(z_0, z_n)\delta\mathbf{T}^{-}(z_n)\mathbf{P}^{-}_{mod}(z_n). \tag{25}$$

This leads to the following:

$$\frac{\partial J_{\Delta}}{\partial\mathbf{R}^{\cup}(z_n)} = -2[\mathbf{W}^{-}(z_0, z_n)]^{H}[\Delta\mathbf{P}(z_0)]\left[\mathbf{P}^{+}_{mod}(z_n)\right]^{H}. \tag{26}$$

Thus, the total gradient driving the update of the reflectivities at each iteration of the algorithm is as follows:

$$\frac{\partial J}{\partial\mathbf{R}^{\cup}(z_n)} \approx [\mathbf{W}^{-}(z_0, z_n)]^{H}[\Delta\mathbf{P}(z_0)]\left[\mathbf{P}^{+}_{mod}(z_n)\right]^{H} + \frac{\partial f(\mathbf{R}^{\cup}(z_n))}{\partial\mathbf{R}^{\cup}(z_n)}. \tag{27}$$

Within this framework, it is possible to introduce the concept of blending by defining the so-called *blending matrix* $\mathbf{\Gamma}_{bl}$ (Berkhout 2008). The observed and modelled data will be updated as follows:

$$\mathbf{P}_{obs}(z_0) \quad \longrightarrow \quad \mathbf{P}_{obs,bl}(z_0); \tag{28}$$

$$\mathbf{P}^{-}_{mod}(z_0) \quad \longrightarrow \quad \mathbf{P}^{-}_{mod}(z_0)\mathbf{\Gamma}_{bl} \quad = \quad \mathbf{P}^{-}_{mod,bl}(z_0). \tag{29}$$

All information about the combination of the different sources of the array to be employed during the DSA blended experiments is encoded in $\mathbf{\Gamma}_{bl}$. Each row of $\mathbf{\Gamma}_{bl}$ corresponds to a different source. Each column refers to a different blended shot record. In case of simple time delays between different shots, the elements of $\mathbf{\Gamma}_{bl}$ are given by $\gamma_{ik} = e^{-j\omega\tau_{ik}}$, where τ_{ik} determines the time delay relative to the ith source for the kth blended experiment, and ω refers to the angular frequency.

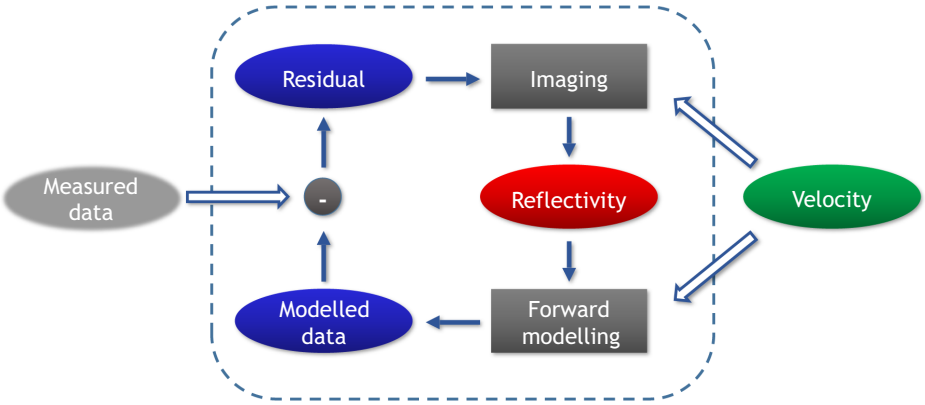

Figure 5 Closed loop for full wavefield migration.

The aforementioned adjustments will lead to a new misfit norm function of the following form:

$$J_{\Delta,bl} = \sum_{\omega} \left\| \Delta \mathbf{P}_{bl}(z_0) \right\|_2^2 = \sum_{\omega} Tr\left(\Delta \mathbf{P}_{bl}(z_0) \Delta \mathbf{P}_{bl}^{H}(z_0) \right), \tag{30}$$

where $\Delta \mathbf{P}_{bl}(z_0)$ is the residual, i.e., the difference between the observed blended data $\mathbf{P}_{obs,bl}(z_0)$ and the modelled blended data $\mathbf{P}^{-}_{mod,bl}(z_0)$, as follows:

$$\Delta \mathbf{P}_{bl}(z_0) = \mathbf{P}_{obs,bl}(z_0) - \mathbf{P}^{-}_{mod,bl}(z_0). \tag{31}$$

Note that no deblending (source separation) is involved in this scheme. It follows that

$$\mathbf{AXB} + \mathbf{C} = \Delta \mathbf{P}_{bl}(z_0); \tag{32}$$

$$\mathbf{A} = -\sum_{n>0} \mathbf{W}^{-}(z_0, z_n); \tag{33}$$

$$\mathbf{X} = \mathbf{R}^{\cup}(z_n); \tag{34}$$

$$\mathbf{B} = \mathbf{P}^{+}_{mod}(z_n) \mathbf{\Gamma}_{bl}; \tag{35}$$

$$\mathbf{C} = \mathbf{P}_{obs,bl}(z_0) - \sum_{n>0} \mathbf{W}^{-}(z_0, z_n) \delta \mathbf{T}^{-}(z_n) \mathbf{P}^{-}_{mod}(z_n) \mathbf{\Gamma}_{bl}. \tag{36}$$

This leads to the following:

$$\frac{\partial J_{\Delta,bl}}{\partial \mathbf{R}^{\cup}(z_n)} = -2[\mathbf{W}^{-}(z_0, z_n)]^{H} [\Delta \mathbf{P}_{bl}(z_0)][\mathbf{\Gamma}_{bl}]^{H} \left[\mathbf{P}^{+}_{mod}(z_n)\right]^{H}. \tag{37}$$

From a physical point of view, we can see the gradient as featured by the following three consecutive steps (see Fig. 6):

(i) Decoding (i.e., *pseudo-deblending*; see Berkhout 2008) of the residual wavefield;

(ii) Back-propagation of the pseudo-deblended residual;

(iii) Cross-correlation of the back-propagated, pseudo-deblended residual wavefield with the forward modelled downgoing wavefield.

NUMERICAL EXAMPLE

In this section, we will demonstrate the feasibility of the dispersed source array (DSA) acquisition method with a 3D numerical example of marine seismic data migration.

The numerical example is based on the 3D SEG EAGE salt model (Aminzadeh *et al.* 1994). The velocity model used as reference is shown in Fig. 7a, whereas the density model is considered to be homogeneous. Note that the three visible sections of the velocity model shown in Fig. 7a portray three orthogonal slices from inside the model. The horizontal slice (top-left) is located at $z = 750$ m. The slice on the bottom-right is located at $x = 1000$ m, and the slice on the bottom-left corner is located at $y = 1000$ m. The model is 2000-m wide along both horizontal directions and 1000 m deep.

The types of DSA sources involved in the acquisition are the ones introduced in the previous sections (see Fig. 1). The source boats sail following straight lines parallel to both horizontal axes. The crossline spacing between neighboring lines is constant and equal to 100 m for the ultralow-frequency sources and 50 m for all other sources. Along the inline direction, the shot interval is irregular in order to distribute the blending noise more uniformly (between 10 m and 20 m for the high-frequency units, between 20 m and 30 m for the mid-frequency units, between 30 m and 70 m for the low-frequency units, and between 50 m and 100 m for the ultralow-frequency units). The sources were fired simultaneously, with a maximum blending fold of four. A number of eight boats were deployed simultaneously for every source type except for the

$$\frac{\partial J_{\Delta,bl}}{\partial \mathbf{R}^{\cup}(z_n)} \approx \left[\mathbf{W}^{-}(z_0, z_n)\right]^H \left[\Delta \mathbf{P}_{bl}(z_0)\right] \left[\mathbf{\Gamma}_{bl}\right]^H \left[\mathbf{P}^{+}_{mod}(z_n)\right]^H$$

1

2

3

Figure 6 Steps for the gradient computation.

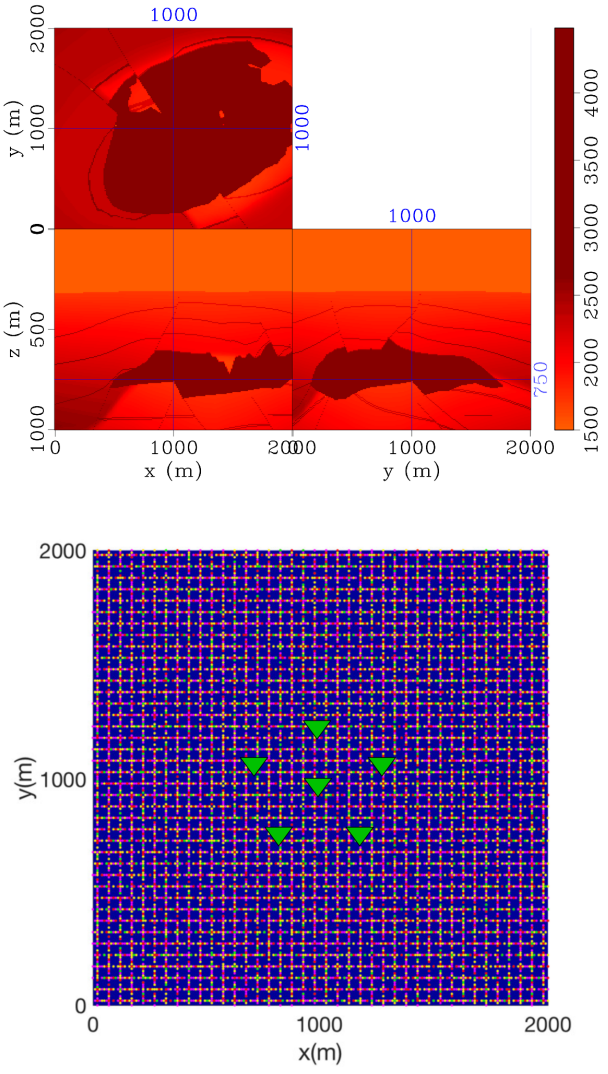

Figure 7 Reference velocity model (a) and schematic illustration of the acquisition geometry (b). Note that the green triangles depict a total of 5 floating nodes evenly spaced along a circumference of 250-m radius around the centre of the area. Each node is positioned at a depth of 250 m below the water surface. The colored dots represent shot locations along straight lines parallel to both horizontal axes. Different colors represent different DSA source types.

ultralow-frequency sources, where four boats were instead deployed. Each source type has been placed at its optimum depth below the water surface, i.e., at $z_s = \lambda_c/4$.

On the receiver side, a total of 5 floating nodes evenly spaced along a circumference of 250-m radius around the centre of the area is chosen. Each node is positioned at a depth of 250 m below the water surface and 50 m above the ocean bottom. In Fig. 7b, an illustrative representation of the acquisition geometry is shown.

The receivers are recording continuously, and the result of this blended experiment is one single *supertrace* per node. The data inversion is performed without preliminary deblending. All internal multiples were utilised and not removed in the inversion process. Figure 8 depicts an example of the continuous signals recorded by the nodes (*supertraces*).

The results of 3D full wave migration algorithm after 1 and 20 iterations of the algorithm are presented in Fig. 9. The same slices for the velocity model are portrayed. With these acquisition settings, we do not expect to properly image the whole model, especially in the larger offsets, but we can see that at the final iteration, the crosstalk and the blending noise are well suppressed.

CONCLUDING REMARKS

Particularly in the last few decades, broadband seismic acquisition has become an increasingly important topic due to its critical importance for high-resolution seismic imaging. Nevertheless, acoustic sources deployed during field surveys are historically chosen to be equal, and as a consequence, it is often inevitable to accept a compromise between wave transmission properties and system engineering complexity. Usually, it is necessary to settle for source sampling intervals and source depths (in marine) that are optimal only for a limited frequency range of the emitted signal.

Replacing the traditional broadband source with multiple devices transmitting a reduced and diversified frequency band offers a wide range of practical advantages, whereas no physical constraint prevents us from employing diverse sources

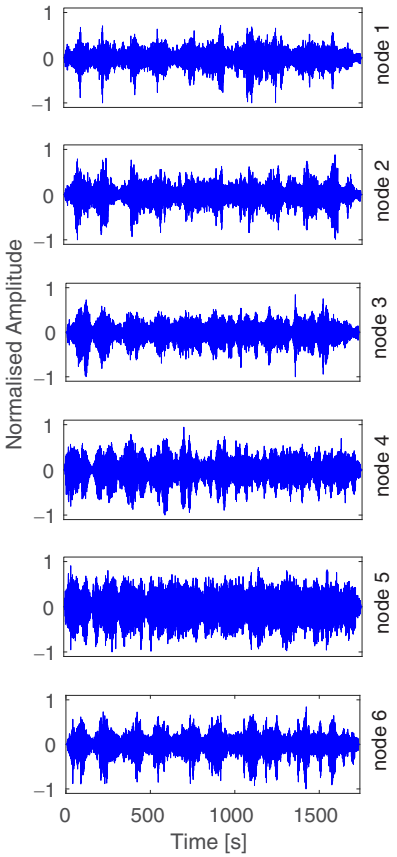

Figure 8 Continuous signals recorded by the nodes (supertraces).

with different spectral properties during seismic surveys. The whole ensemble of sources will be referred to as dispersed source array (DSA).

These sources can be technically simpler to produce and more effective from an energy transmission point of view. Their utilisation will allow shot densities to be chosen in a frequency-dependent manner. Lower frequency source units can be distributed more sparsely, provided that the signal-to-noise ratio is adequate. Smaller and less powerful source units may be adopted densely for the production of the higher frequencies, reducing the complexity and increasing the operational flexibility of the system, as well as mitigating its environmental impact. Furthermore, in marine surveys, the concept offers the possibility to tow the devices at depths that are optimum for their specific frequency range, giving extra benefits if we look at the source ghost issue. The destructive interference due to the ghost notches and the low-frequency attenuation due to shallow tow depths are largely avoided.

Interesting and encouraging migration results from 3D blended DSA data have been produced with no deblending (source separation) involved in the inversion scheme.

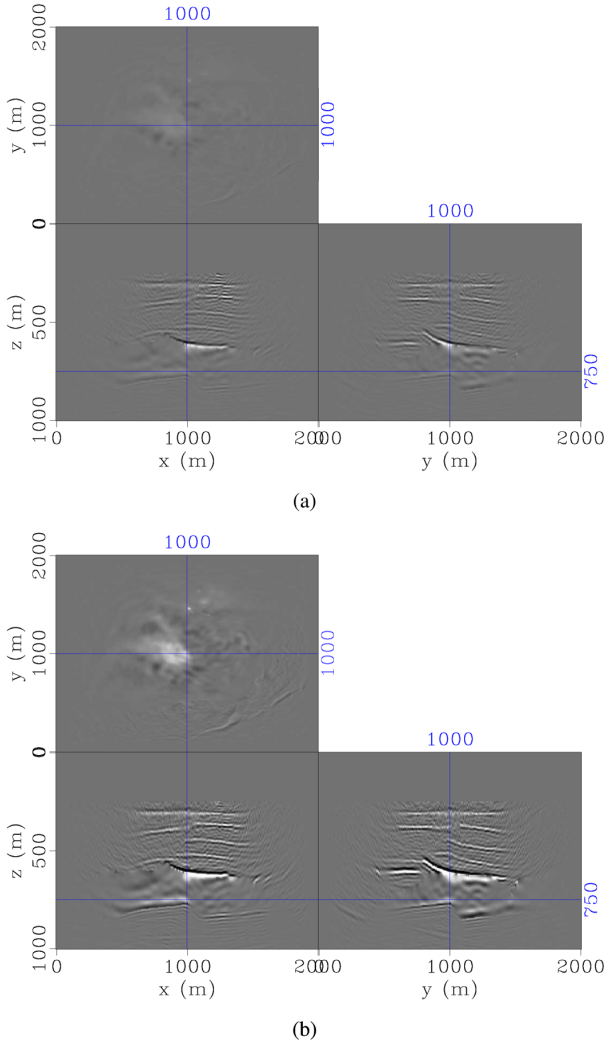

Figure 9 Three-dimensional images after 1 full wavefield migration iteration (a) and after 20 full wavefield migration iterations (b).

ACKNOWLEDGEMENTS

The authors would like to thank the sponsors of the Delphi consortium for the stimulating discussions during the Delphi meetings and their continuous financial support.

REFERENCES

Aminzadeh F., Burkhard J.M., Nicoletis L., Rocca F. and Wyatt K. 1994. SEG/EAGE 3D modeling project: second update. *The Leading Edge* **13**(9), 949–952.

Amundsen L., Røsten T., Robertsson J.O.A. and Kragh E. 2005. Rough-sea deghosting of streamer seismic data using pressure gradient approximations. *Geophysics* **70**(1), V1–V9.

Berkhout A.J. 1982. Seismic Migration, Imaging of Acoustic Energy by Wave Field Extrapolation, A: Theoretical Aspects, Elsevier

Berkhout A.J. 2008. Changing the mindset in seismic acquisition. *The Leading Edge* **27**(7), 924–938.

Berkhout A.J. 2012. Blended acquisition with dispersed source arrays. *Geophysics* **77**(4), A19–A23.

Berkhout A.J. 2014a. Review paper: an outlook on the future seismic imaging, part I: forward and reverse modelling. *Geophysical Prospecting* **62**(5), 911–930.

Berkhout A.J. 2014b. Review paper: an outlook on the future seismic imaging, part II: full-wavefield migration. *Geophysical Prospecting* **62**(5), 931–949.

Caporal M., Blacquière G. and Davydenko M. 2016. 3D seismic acquisition with decentralized dispersed source arrays. 86th SEG annual international meeting, Expanded Abstracts.

Coste E., Gerez D., Groenaas H., Hopperstad J.F., Pramm Larsen O., Laws R. *et al.* 2014. Attenuated high-frequency emission from a new design of air-gun. 84th SEG annual international meeting, Expanded Abstracts.

Davis D. and Patronis E. 2006. *Sound System Engineering*, Focal Press.

Davydenko M. and Verschuur D.J. 2017. Full-wavefield migration: using surface and internal multiples in imaging. *Geophysical Prospecting* **65**(1), 7–21.

Dellinger J., Ross A., Meaux D., Brenders A., Gesoff G., Etgen J.T. *et al.* 2016. Wolfspar, an FWI friendly ultra-low-frequency marine seismic source. 86th SEG annual international meeting, Expanded Abstracts.

Duncan A.J., Weilgart L., Leaper R., Jasny M. and Livermore S. 2017. A modeling comparison between received sound levels produced by a marine vibroseis array and those from an airgun array for some typical survey scenarios. *Marine Pollution Bulletin* **119**(1), 277–288.

Erbe C., Sisneros J., Thomsen F., Hawkins A. and Popper A. 2016. Overview of the 4th international conference on the effects of noise on aquatic life. *Proceedings of Meetings on Acoustics*, Vol. 27, p. 040006.

European Union. 2008. Directive 2008/56/ec of the european parliament and of the council of 17 june 2008 establishing a framework for community action in the field of marine environmental policy (marine strategy framework directive). *Official Journal of the European Union* **L 164**, 19–40.

Fontana P.M. and Zickerman P. 2010. Mitigating the environmental footprint of towed streamer seismic surveys. *First Break* **28**(12), 57–63.

Kragh E., Laws R., Hopperstad J.F. and Kireev A. 2012. Reducing the size of the seismic source with a 4C towed-marine streamer. 74th EAGE annual international meeting, Expanded Abstracts.

Kunc H.P., McLaughlin K.E. and Schmidt R. 2016. Aquatic noise pollution: implications for individuals, populations, and ecosystems. *Proceedings of the Royal Society of London B*, Vol. 283, pp. 20160839.

Laiolo P. 2010, The emerging significance of bioacoustics in animal species conservation. *Biological Conservation* **143**, 1635–1645.

Laws R. and Kragh E. 2002. Rough seas and time-lapse seismic. *Geophysical Prospecting* **50**(2), 195–208.

Laws R.M., Kragh E. and Morgan G. 2008. Are seismic sources too loud? 70th EAGE annual international meeting, Expanded Abstracts.

Madsen P.T., Johnson M., Miller P.J.O., Soto N.A., Lynch J. and Tyack P. 2006. Quantitative measures of air-gun pulses recorded on sperm whales (physeter macrocephalus) using acoustic tags during controlled exposure experiments. *Journal Acoustical Society of America* **120**(4), 2366–2379.

MSFD. 2014. Monitoring guidance for underwater noise in European seas. In: *JRC Scientific and policy reports*. Marine Strategy Framework Directive (MSFD) - Technical Subgroup on Underwater Noise.

Niland R.A. 1989. Optimum oversampling. *Journal Acoustical Society of America* **86**(5), 1805–1812.

NOAA. 2016. Technical guidance for assessing the effects of anthropogenic sound on marine mammal hearing: underwater acoustic thresholds for onset of permanent and temporary threshold shifts. NOAA Technical Memorandum NMFS-OPR-55. US Department of Commerce and National Oceanic and Atmospheric Administration (NOAA) and National Marine Fisheries Service (NMFS).

Nowacek D.P., Thorne L.H., Johnston D.W. and Tyack P.L. 2007. Responses of cetaceans to anthropogenic noise. *Mammal Review* **37**(2), 81–115.

Orji O.C., Söllner W. and Gelius L.J. 2012. Effects of time-varying sea surface in marine seismic data. *Geophysics* **77**(3), P33–P43.

Parkes G. and Hatton L. 1986. *The Marine Seismic Source*. Reidel.

Petersen K.B. and Pedersen M.S. 2012. *Matrix Cookbook*. Technical University of Denmark.

Reust D.K., Johnston O.A., Giles J.A., and Ballinger S. 2015. Very low frequency seismic source. 85th SEG annual international meeting, Expanded Abstracts.

Shannon G., McKenna M.F., Angeloni L.M., Crooks K.R., Fristrup K.M., Brown E. *et al.* 2016. A synthesis of two decades of research documenting the effects of noise on wildlife. *Biological Reviews* **91**, 982–1005.

Shen H., Elboth T., Tian G., Warszawski J. and Lilja D. 2014, Theoretical study on multilevel source design. *Geophysical Prospecting* **62**(6), 1337–1352.

Southall B.L., Bowles A.E., Ellison W.T., Finneran J.J., Gentry R.L., Greene Jr. C.R. *et al.* 2007. Marine mammal noise exposure criteria: initial scientific recommendations. *Aquatic Mammals* **33**(4), 411–521.

Tanner W.P. 1958. What is masking? *Journal Acoustical Society of America* **30**(10), 919–921.

ten Kroode F., Bergler S., Corsten C., de Maag J.W., Strijbos F. and Tijhof H. 2013. Broadband seismic data—The importance of low frequencies. *Geophysics* **78**(2), WA3–WA14.

Tsingas C., Kim Y.S. and Yoo J. 2016. Broadband acquisition, deblending, and imaging employing dispersed source arrays. *The Leading Edge* **35**(4), 354–360.